Adaptive Totem Pole PFC Control Based on Backpropagation Neural Network With Wide Voltage Range and Low Current THD

Hao Chu, Jiajia Guan, *Member, IEEE*, Xuchen Sun, Xiangan Xiao, Letian Tong, Xinyu He, *Student Member, IEEE*, Cai Chen, *Member, IEEE*, and Yong Kang, *Fellow, IEEE*

***Abstract*—The totem pole power factor correction (PFC) circuit is a prevalent front-end topology employed in on-board chargers owing to its high efficiency and uncomplicated structure. Nevertheless, the conventional fixed parameters control methods are deficient in terms of robustness, resulting in high total harmonic distortion (THD) of input current when operating over a wide voltage range. To solve this problem, this article first proposes a dynamic root locus PI control based on the small signal model analysis of totem pole PFC. Furthermore, a dual-frequency adaptive PI control based on back propagation neural networks (DF-BPPI) is proposed for optimization of the control parameters. Compared to existing methods, the proposed control method can achieve lower current THD under different output voltages and loads. Experimental results on a 3-kW prototype demonstrate that the proposed DF-BPPI control attains a THD of less than 3% and a power factor higher than 0.995 under all output voltages above half load.**

***Index Terms*—Adaptive control, backpropagation neural network, low current total harmonic distortion (THD), Totem pole power factor correction (PFC).**

NOMENCLATURE

Parameters	Description.
V_{in}	Input voltage.
V_o	Output voltage.
C_o, R_L, L	Circuit resistance, capacitance and inductance.
i_L	Current of inductance.
D	Duty cycle.
$\hat{x}$, $\hat{d}$, $\hat{u}$	Small disturbance momentum.
G_{id}	Transfer function from duty cycle to input inductor current.
A_r	Sinusoidal pulse width modulation reference.
PI	Proportional and integral control.
K_p, K_i	Continuous domain PI parameters
K_p', K_i'	Discrete domain PI parameters.
K_E	Evans' gain value.
$S_X^T(s)$	Sensitivity to variable X.
l_1, l_2	The distance from the closed-loop pole to the open-loop zero and the open-loop pole.
ξ	Damping ratio.
P_0, Z_0	Open-loop pole, open-loop zero.
α, β	Inertia coefficient and learning rate.
DRL-PI	Dynamic root locus PI control.
DF-BPPI	Dual-frequency adaptive PI control based on back propagation neural network.
O_i, O_j, O_k	Input layer, hidden layer, and output layer.
w_{ij}, w_{jk}	Connection weights between neurons.
net_j, net_k	Weighted summation layer.
Δw_{ij}, Δw_{jk}	Weight variation.
$e(n)_{\max}$	Maximum current error.
$\overline{E}(m)$	Mean square error.
$i*$	Current rms instruction.
$f(x)$	Tanh activation function.

Received 1 July 2025; revised 29 September 2025; accepted 7 November 2025. Date of publication 14 November 2025; date of current version 19 January 2026. Recommended for publication by Associate Editor S. S. Lee. *(Corresponding author: Jiajia Guan.)*

The authors are with the School of Electrical and Electronic Engineering, Huazhong University of Science and Technology, Wuhan 430074, China (e-mail: hao_chu@hust.edu.cn; jiajiaguan@hust.edu.cn; xvchen315@hust.edu.cn; M202572411@hust.edu.cn; d202180640@alumni.hust.edu.cn; M202472506@hust.edu.cn; caichen@hust.edu.cn; ykyang@hust.edu.cn).

Color versions of one or more figures in this article are available at https://doi.org/10.1109/TPEL.2025.3632975.

Digital Object Identifier 10.1109/TPEL.2025.3632975

I. INTRODUCTION

WITH the development of the global economy, the energy crisis has become one of the most significant challenges faced by humanity, leading to an increasing demand for electrified transportation systems [1]. As an important component of electric vehicles (EVs) and plug-in hybrid electric vehicles, the on-board charger (OBC) holds substantial application potential [2]. The typical structure of two-stage type OBC is shown in Fig. 1. Among various topologies, the totem pole power factor correction (PFC) circuit has garnered extensive research and practical application as the prestage ac/dc converter due to its high power factor (PF), simple structure, and low switching losses [3], [4], [5].

The voltage of a single cell in the EV typically ranges from 2.5 to 4.2 V [6], [7], leading to significant variations in the required charging voltage for the battery pack. In order to accommodate this wide voltage range and achieve higher overall efficiency, the two-stage OBC imposes requirements on the voltage regulation capabilities of its totem pole PFC circuit [8], [9]. Furthermore, traditional controllers are not robust against external disturbances and uncertainties. Changes in key circuit parameters due to environmental factors will render preset control parameters ineffective, leading to an increase in current total harmonic

TABLE I
COMPARISON BETWEEN DIFFERENT CONTROL METHODS

Controller	Advantages	Disadvantages	Robustness	Feasibility
PI [12]	1. Simple structure, easy to implement and tune. 2. Intuitive concept, widely used and well-understood.	1. Poor performance for nonlinear, strongly coupled systems. 2. Fixed parameters offer limited ability to handle model uncertainties.	Poor	High
LQR [13]	1. Optimal control for multi-variable systems based on a state-space model. 2. Theoretically guarantees stability and some degree of robustness	1. The adjustability is limited to a narrow area around the operating point. 2. Highly dependent on an accurate model.	Moderate	High
PI-Fuzzy [14]	1. No exact model needed, relies on expert knowledge. 2. Adaptive with online tuning capability.	1. Complex design of rules and membership functions. 2. Perform limited by the rule base.	Moderate	High
Sliding mode [15]	1. Fast response and good convergence. 2. Invariant to disturbances on the sliding surface	1. Chattering leads to system power loss.	Moderate	High
HOSMC [16]	1. Strong robustness. 2. Reduce or eliminate chattering.	1. Difficult to realize. 2. High computational requirements.	Excellent	Low
Single-neuron feedback PI [20], [21], [22]	1. Simple structure, low computational load. 2. Self-learning, can adapt parameters online.	The gain mainly depends on the empirical method, which limits its adaptability.	Moderate	High
BP-PID [23]	1. Powerful nonlinear mapping capability. 2. Learn the optimal strategy through online training.	1. High computational demands. 2. Susceptibility to local optima and excessive overshoot.	Excellent	Low
Proposed DF-BPPI	1. Suitable for real-time control of power electronics. 2. Lower computing resource requirements. 3. Excellent adaptive ability and nonlinear mapping ability.	1. More complex than PI control. 2. Need to establish a simplified control model.	Excellent	High

distortion (THD) [10]. The international standards, such as IEC 61000-3-2, impose stringent requirements on the current THD of electrical equipment. The increased harmonic current will increase power grid loss and harmonic pollution, and reduce power grid capacity utilization and energy efficiency [11]. These challenges emphasize the urgency of researching adaptive control methods for totem pole PFC over a wide output voltage range. Although the traditional double-loop proportional integral (PI) controller [12] has been widely used in PFC applications due to its relatively simple control logic, it is difficult to achieve an effective balance between fast response and precise control over a wide operating range. Some studies have explored linear quadratic regulation (LQR) control [13], but the adjustability of this method is limited to a narrow area around the operating point. The fuzzy PI controller is also an effective method for implementing adaptive control, but the design of its rules heavily relies on empirical knowledge [14]. Literature also reports the use of sliding mode controllers based on Lyapunov functions in PFC control [15], which exhibits robustness to uncertainties but may introduce chattering that leads to system power loss. The high-order sliding mode (HOSMC) control method is considered a promising adaptive control method, but its practical implementation remains challenging due to its high complexity [16].

In recent years, the rapid development of artificial intelligence (AI) has led to the emergence of hybrid control methods combining AI with traditional control methods, which have been experimentally validated in various fields [17], [18], [19]. The single-neuron feedback PI network, characterized by its simplicity and online parameter adjustment capabilities, has demonstrated practical value in applications such as remote sensing platform control [20] and controlled nuclear fusion [21]. However, its overall gain primarily relies on empirical methods, which limit its adaptability [22]. Furthermore, researchers designed a PID control method based on back propagation (BP), known as the BP-PID method [23]. This method has achieved success in diverse areas such as three-phase PWM rectifier control [24], turbine unit control [25], and robot arm control [26], demonstrating excellent adaptability to complex nonlinear systems and dynamic environments. However, the BP-PID method faces challenges such as high computational demands, susceptibility to local optima, and excessive overshoot during control processes, making it less suitable for electronic converter control [27]. Therefore, this method needs to be improved to make it more suitable for controlling the totem pole PFC model. Table I shows the advantages and disadvantages of the literature scheme investigated. The main work and contributions of this article are as follows:

1) The theoretical small signal model of totem pole PFC is established, and a dynamic root locus PI (DRL-PI) control method suitable for wide voltage and load range control is proposed. Realize low current THD of totem pole PFC in a wide range of output voltage and load.

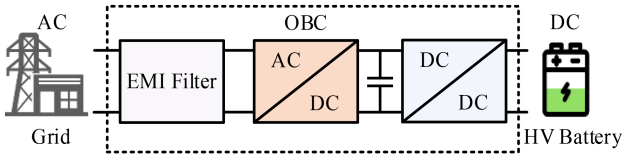

Fig. 1. Typical structure of OBC.

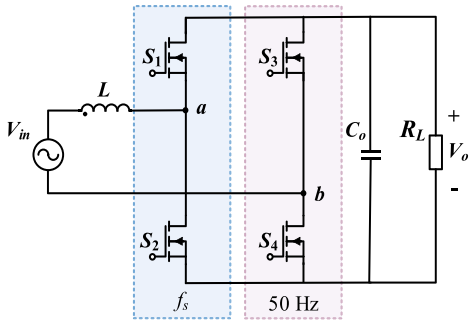

Fig. 2. Topology of totem pole PFC.

2) To address the inaccuracies inherent in the theoretical model, a dual-frequency adaptive BP-PI control method (DF-BPPI) is proposed. The proposed method solves the problem that the traditional BP-PID algorithm has a large amount of calculation and is sensitive to the local optimal solution, realizes a wide range of adaptive adjustment, and significantly reduces the current THD.
3) The robustness of the proposed control is verified based on a 3-kW prototype, achieving lower current THD under all operating output voltages and loads.

The rest of this article is as follows. Section II describes the establishment of small signal model for totem pole PFC, and proposes the DRL-PI control method. Section III proposes the DF-BPPI control method to achieve adaptive control. Section IV designs a 3-kW prototype and verifies the proposed DF-BPPI control method. Finally, Section V concludes this article.

II. Totem Pole PFC Control Model and DRL-PI

A. Large and Small Signal Model Analysis

The topology of totem pole PFC is shown in Fig. 2. The converter consists of inductor L, output capacitor C_o, output load R_L, high frequency switching tubes S_1, S_2 and low frequency switching tubes S_3, S_4. Fig. 3 shows the switching waveforms.

When the ac input voltage is under a positive half cycle, the operating state is shown in Fig. 4(a) and (b). During this stage, switching tube S_3 is OFF and S_4 is ON. In the operating state shown in Fig. 4(a), S_1 is OFF and S_2 is ON, allowing the ac input to charge the inductor. At the same time, the capacitor supplies power to the output load, causing the output voltage to decrease. In the operating state shown in Fig. 4(b), S_1 is ON and S_2 is OFF, causing the inductor to discharge. The input voltage and the inductor voltage are superimposed, simultaneously charging the capacitor and powering the load, resulting in an increase in the output voltage. When the ac input voltage is under a negative

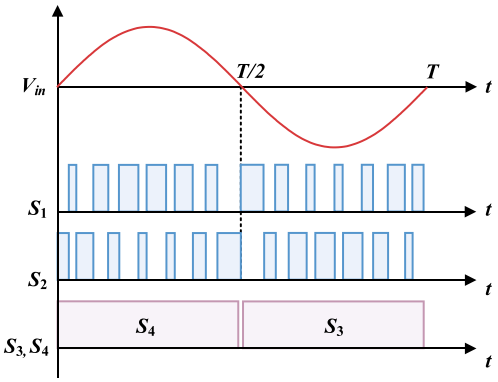

Fig. 3. Switching waveform of the totem pole PFC.

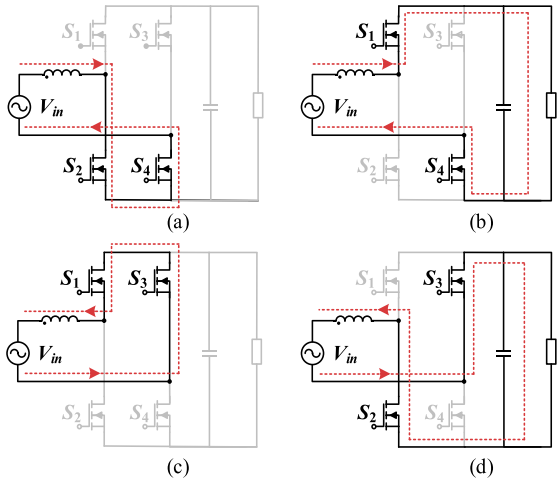

Fig. 4. Operation process stages of totem pole PFC. (a) Inductive charging under positive half cycle. (b) Inductive discharge under positive half cycle. (c) Inductive charging under negative half cycle. (d) Inductive discharge under negative half cycle.

half cycle, the operating states are shown in Fig. 4(c) and (d), where the switching tubes S_3 and S_4 operate in the opposite way to that described above. The analysis of these two operating states is similar to the states analysis above. During the negative half-cycle, the inductor is charged when S_1 is conducting and discharged when S_1 is not conducting.

Given the symmetrical operating characteristics of totem pole PFC in both the positive and negative half-cycles of the input voltage, this article examines the positive half-cycle as a representative example. The state space equation is adopted to analyze the large signal model of totem pole PFC within a switching cycle, thereby providing a unified mathematical model of the system. This approach facilitates subsequent analysis and optimization. The developed state space equation is as follows:

$$\dot{X} = AX + BU, X = \begin{bmatrix} i_L \\ V_o \end{bmatrix}, U = [V_{\text{in}}] \tag{1}$$

where i_L is the inductive current. For a complete cycle, the state equation of the totem pole PFC large signal model within a

switching period is

$$\dot{X} = AX + BU, A = \begin{bmatrix} 0 & -\frac{1-D}{L} \\ \frac{1-D}{C_o} & -\frac{1}{R_L C_o} \end{bmatrix}, B = \begin{bmatrix} 1/L \\ 0 \end{bmatrix} \quad (2)$$

where D is the duty cycle.

Small signal model is a common analysis method in power electronics. By linearizing nonlinear circuits, the analysis of circuits becomes more intuitive. In this article, the perturbation method is used to build a small signal model of totem pole PFC. Based on the large signal model, add small perturbations $\hat{x}$, $\hat{d}$, and $\hat{u}$, and the equation after applying the perturbations is as follows:

$$\begin{aligned} \dot{X} + \dot{\hat{x}} = & \left[\left(D + \hat{d}\right) A_1 + \left(1 - D - \hat{d}\right) A_2\right] (X + \hat{x}) \\ & + \left[\left(D + \hat{d}\right) B_1 + \left(1 - D - \hat{d}\right) B_2\right] (U + \hat{u}). \end{aligned} \quad (3)$$

Disregarding second-order small quantities, the steady-state (4) and the small signal model (5) are separated

$$\dot{X} = [DA_1 + (1-D)A_2]X + [DB_1 + (1-D)B_2]U \quad (4)$$

$$\dot{\hat{x}} = A\hat{x} + B\hat{u} + [(A_1 - A_2)X + (B_1 - B_2)U]\hat{d}. \quad (5)$$

In double-loop control, the inner current loop ensures that the input current is close to the sinusoidal waveform, which is the main factor affecting the input current THD and PF. In order to reduce the current THD, the following analysis in this article will focus on the control of the inner current loop.

Considering that the system is in a steady state, the effect of the feedforward loop can be ignored. The transfer function from duty cycle to input inductor current can be derived by the Laplace transform of (5)

$$G_{id} = \frac{V_o C_o R_L s + 2V_o}{LC_o R_L s^2 + Ls + (1-D)^2 R_L}. \quad (6)$$

The converter designed in this article operates at a switching frequency of 75 kHz. As mentioned in [28], the analysis of the transfer function of the current loop focuses on the high-frequency response characteristics. The transfer function can be simplified as follows:

$$G_{id} = \frac{V_o}{Ls}. \quad (7)$$

The Bode diagram in Fig. 5 shows the frequency response of the transfer function before and after simplification. In the high-frequency region, the simplified transfer function closely matches the original transfer function, indicating that the simplified analysis is applicable to the high-frequency response.

B. PI Control Based on Dynamic Root Locus

Fig. 6 shows the traditional double-loop control method, where PLL is the phase-locked loop and A_r is the sinusoidal pulsewidth modulation reference. This method adopts a combination of a voltage outer loop and a current inner loop, and introduces feedforward to accelerate response and stabilize the system.

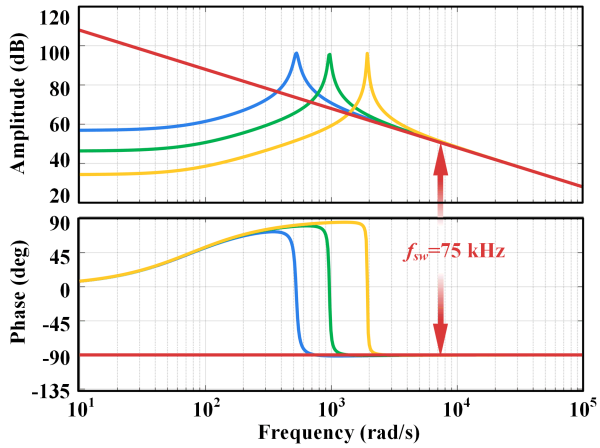

Fig. 5. Comparison of Bode diagram before and after simplification.

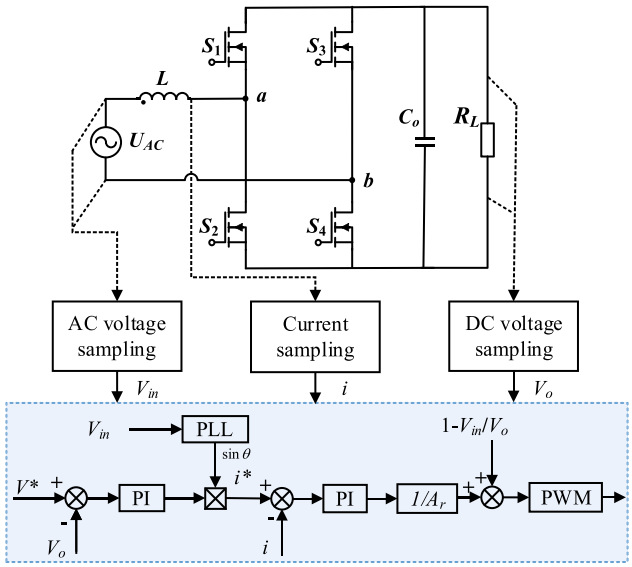

Fig. 6. Traditional control block diagram.

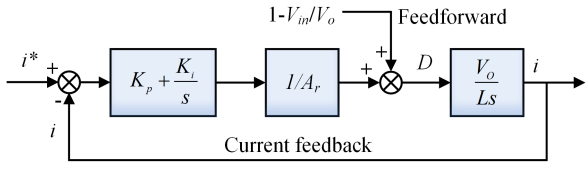

Fig. 7. Control block diagram of the traditional current inner loop.

By combining (7) with the PI controller transfer function, the control block diagram of the current inner loop can be obtained as shown in Fig. 7. The open-loop transfer function expressed in Evans' form is

$$\mathrm{GH}(s) = \left(\frac{s + K_i/K_p}{s^2}\right) \cdot \frac{K_p V_o}{A_r L} \quad (8)$$

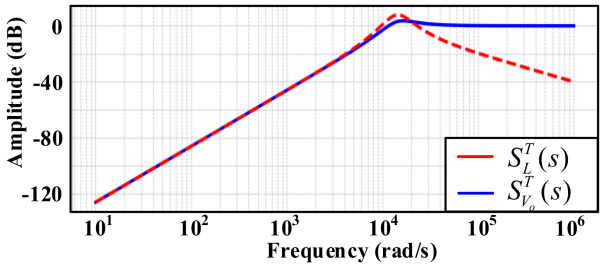

Fig. 8. Bode diagram of system sensitivity.

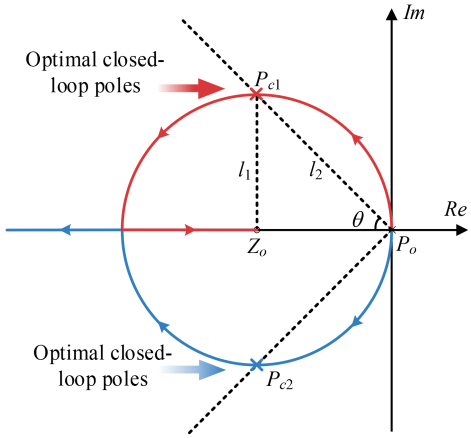

Fig. 9. Root locus curve of the inner current loop.

where K_p is the proportional coefficient, K_i is the integral coefficient, and the Evans' gain value can be expressed as

$$K_E = \frac{K_p V_o}{A_r L}. \tag{9}$$

The closed-loop transfer function is

$$T(s) = \frac{\mathrm{GH}(s)}{1 + \mathrm{GH}(s)}. \tag{10}$$

The sensitivity analysis is conducted to quantitatively evaluate the robustness of the proposed method. The sensitivity functions of the closed-loop system to the output voltage and inductance are as follows:

$$S_{V_o}^T(s) = \frac{\partial T(s)/T(s)}{\partial V_o/V_o} = \frac{1}{1 + \mathrm{GH}(s)} \tag{11}$$

$$S_L^T(s) = \frac{\partial T(s)/T(s)}{\partial L/L} = -\frac{\mathrm{GH}(s)}{(1 + \mathrm{GH}(s))^2}. \tag{12}$$

Fig. 8 shows the Bode plot of system sensitivity. In a wide range of frequencies, the Bode gain of sensitivity is not zero, so the system is sensitive to changes in voltage and inductance. Fixed parameter control is not suitable for a wide range control.

The root locus is shown in Fig. 9, where there are two open-loop poles P_0 and one open-loop zero Z_0 (-K_i / K_p, 0), and the directions of the two root locus branches are marked in the figure. For a given value of Evans' gain, P_{c1} and P_{c2} are two closed-loop poles, l_1 is the distance from the closed-loop pole

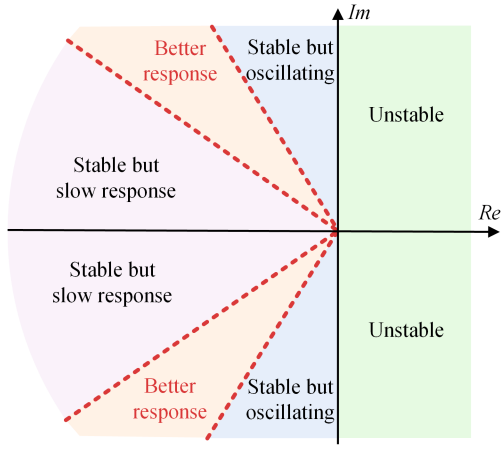

Fig. 10. Relationship between closed-loop poles and response.

to the open-loop zero and l_2 is the distance from the closed-loop pole to the open-loop pole. In the circumstances, Evans' gain and damping ratio ξ satisfy

$$K_E = \frac{l_2 \cdot l_2}{l_1} \tag{13}$$

$$\xi = \cos(\theta). \tag{14}$$

Fig. 10 shows the relationship between the selection of closed-loop poles and the response in the design of the root locus. The change in output voltage will cause a change in the zero position of the open-loop, which further leads to a change in the root locus. The emergence of dynamic root trajectories means that the stability and dynamic response characteristics of the system are no longer constant. In this case, a fixed parameter PI controller is difficult to consistently operate the system within the optimal performance range.

For closed-loop systems, $\xi = 0.707$ is often used as a design guideline [29]. At this damping ratio, the closed-loop poles are within the optimal response range, which means the system has faster response and lower overshoot. For the system analyzed in this article, this means

$$\theta = 45^\circ. \tag{15}$$

$$l_1 = -K_i/K_p = l_2/\sqrt{2}. \tag{16}$$

Simultaneously (9), (13), and (16), the PI controller parameters satisfy

$$\frac{{K_p}^2}{K_i} = \frac{2A_r L}{V_o}. \tag{17}$$

In order to achieve faster system response, it is necessary to select a sufficiently large attenuation index. In the dynamic root locus design in this article, the attenuation index is selected as $\xi\,\omega_n = 10^4$, which satisfies:

$$K_i/K_p = \xi\omega_n. \tag{18}$$

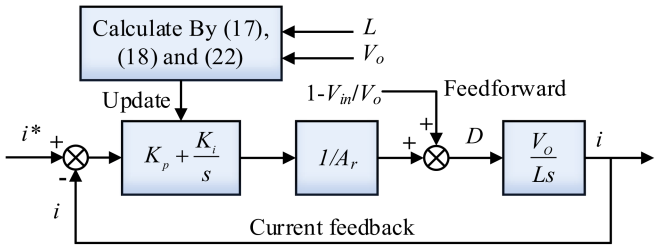

Fig. 11. Proposed DRL-PI control block diagram.

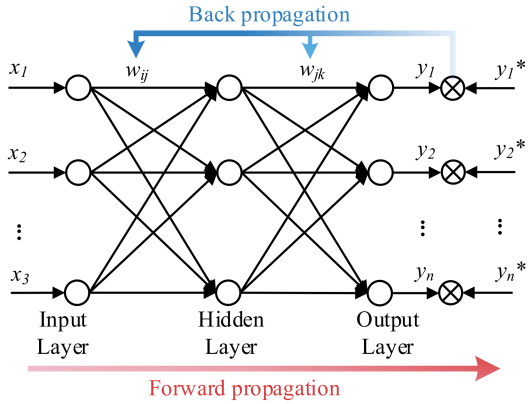

Fig. 12. BP neural network model.

Equations (17) and (18) demonstrate the relationship between the circuit parameters, output voltage, and optimal control parameters of the PI controller in the continuous time domain. The analysis clearly indicates that the control parameters are primarily determined by the inductance and output voltage. Based on this understanding, this section proposes a DRL-PI control method, illustrated in Fig. 11. The DRL-PI continuously adjusts the PI parameters according to the variations in inductance and output voltage using the derived equations, thereby enhancing the system's adaptability to condition changes. The sensitivity analysis is as follows:

$$S_{V_o}^{T}(s) = \frac{\partial T(s)/T(s)}{\partial V_o/V_o} = 0 \tag{19}$$

$$S_{L}^{T}(s) = \frac{\partial T(s)/T(s)}{\partial L/L} = 0. \tag{20}$$

The sensitivity of the system to variations in output voltage and inductance approaches zero under the proposed control method. This indicates that the enhanced system exhibits strong robustness against fluctuations in these parameters, demonstrating the adaptive capability of the new controller.

Considering the actual control of the digital signal processor, the time domain expression is discretized to obtain the parameters of the digital signal controller. The backward Euler method is a common discretization method. It possesses the advantages of constant steady-state gain before and after the transformation, and the performance of the discretized system is similar to that of the prediscretization system when the frequency is high [30]. The incremental PI algorithm is expressed as follows:

$$\Delta U = K_p(E(n) - E(n-1)) + TK_iE(n) \tag{21}$$

where E is the error, T is the control period, and ΔU is the output increment value for each control.

The relationship between PI parameters in the digital controller and the continuous time domain is as follows:

$$\begin{cases} K_p' = K_p \\ K_i' = TK_i \end{cases}. \tag{22}$$

As illustrated by (17), (18), and (22), the optimal control parameters derived from the theoretical model in discrete form can be obtained. In addition, the proposed control method is applicable to both continuous conduction mode and critical conduction mode, without an additional mode switching mechanism. The substitution of the inductance value and the target output voltage into the function enables the continuous adjustment of the PI parameters, thereby ensuring that the current inner loop attains lower THD over a wide voltage range.

III. Proposed DF-BPPI Control

Although the previous analysis provides a simplified theoretical framework, it does not consider the influence of parasitic parameters, sampling time, temperature changes, and other factors in the circuit. The error of the theoretical model will lead to the incomplete optimization of the theoretical control parameters. Therefore, while the proposed DRL-PI method shows preliminary success in voltage adaptive control, its performance requires further improvement. In this section, a dual-frequency adaptive PI control based on backpropagation neural network (DF-BPPI) is proposed. This method introduces an online parameter optimization neural network into the DRL-PI control, improving the adaptability of the system and achieving a low THD of current.

A. Dual-Frequency Backpropagation Neural Network Suitable for the Totem Pole PFC

A backpropagation neural network is a feedforward neural network trained according to the error backpropagation algorithm, which consists of one input layer, several hidden layers, and one output layer. The learning process involves two main steps: forward propagation and backpropagation. In the forward propagation process, the normalization parameters are fed into the neural network and calculated based on connection weights, activation functions, and node thresholds at each layer. When there is an error between the output value and the expected value, backpropagation is performed to adjust the weights and minimize the error. The common framework structure of the BP neural network is shown in Fig. 12.

In order to achieve low current THD under all operating conditions, this article improves the traditional BP neural network and forms a new structure suitable for inner loop control of PFC, as shown in Fig. 13. The further control block diagram of the proposed DF-BPPI is illustrated in Fig. 14. The whole system adopts the strategy of online learning. The data used for

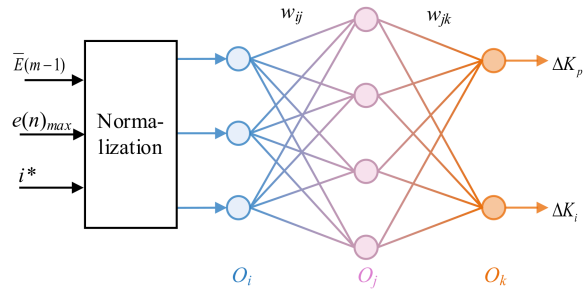

Fig. 13. Backpropagation neural network for PFC control designed in this article.

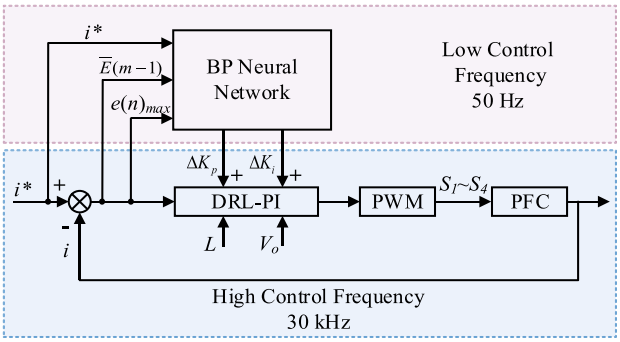

Fig. 14. Proposed DF-BPPI control block diagram.

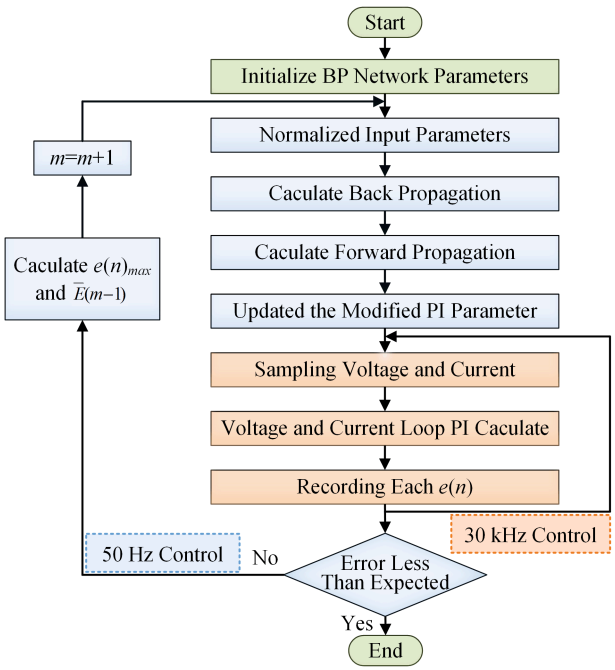

Fig. 15. Proposed DF-BPPI flowchart.

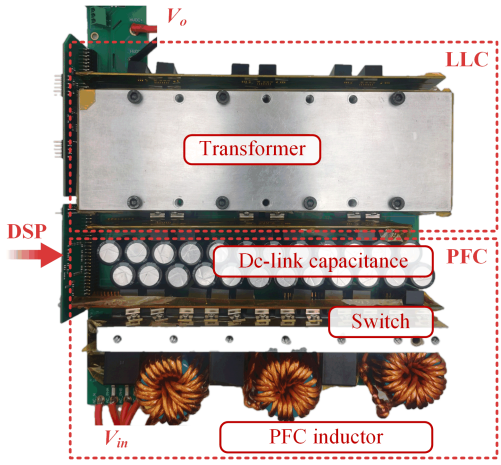

Fig. 16. Prototype of the OBC.

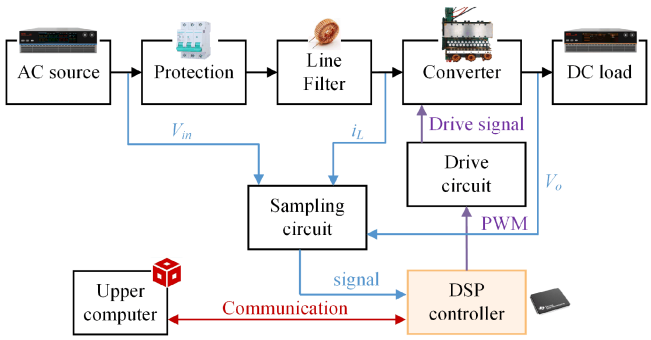

Fig. 17. Hardware connection block diagram.

training is the real-time data collected by voltage and current sampling, and there is no need to provide additional offline data sets. With the continuous operation of the system, more data will enter the model for continuous training, and the model will be continuously updated during operation. The design of the neural network includes three layers of nodes, and the number of neurons in each layer is 3, 4, and 2. O_i, O_j, and O_k are the input layer, hidden layer, and output layer of the network, respectively, w_{ij} and w_{jk} are the connection weights between neurons. The key data of the totem pole PFC rectifier in one utility frequency cycle are selected as the inputs of the neural network, including the maximum current error $e(n)_{\max}$, the mean square error $\bar{E}(m-1)$, and the current rms instruction i^*. In particular, this article uses n to represent the number of calculation periods and m to represent the number of utility frequency periods. These input data are normalized to improve the training efficiency and prediction accuracy of the neural network. For the main structure of the neural network, four hidden-layer neuron nodes and two output-layer neuron nodes are set up. These two output nodes respectively correspond to the parameter correction of the PI controller. Different from the traditional BP-PID, the network designed in this article modifies the parameters based on the DRL-PI control proposed in Section II, reducing the influence of network oscillation on the circuit control and improving the response speed of the network.

Furthermore, a dual frequency control method integrating fast and slow control frequency components is designed in this article to address the problem of slow calculation speed and inability to adapt to ac current control in traditional BP-PID. This method divides the control process into two modules: low-frequency

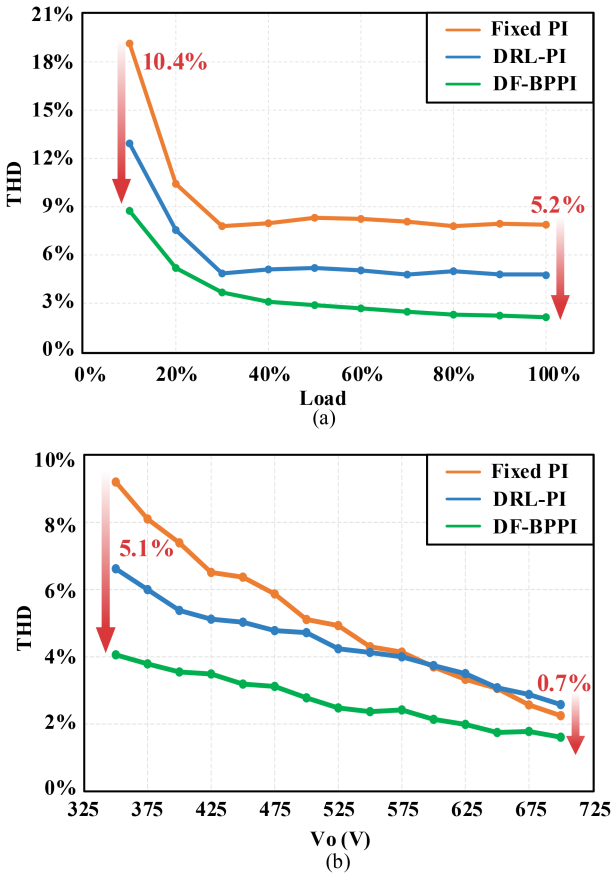

Fig. 18. Experimental results of THD comparison of different control methods. (a) Different loads at $V_o = 400$ V. (b) Different output voltages at $R_L = 160$ Ω.

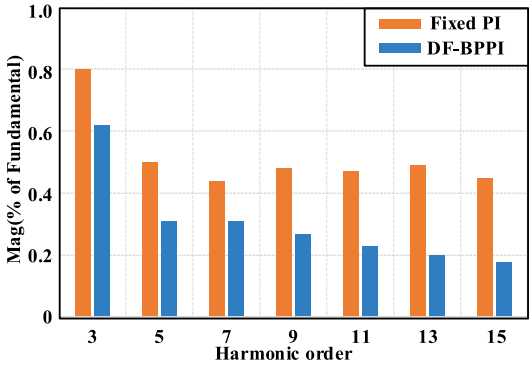

Fig. 19. Harmonic component comparison at full load at $V_o = 700$ V.

and high-frequency. The low-frequency module operates during the utility frequency cycles, focusing on intelligent adjustment and optimization of controller parameters by above BP neural network. This means that the interrupt frequency calculated by the neural network is the utility frequency. The high-frequency module operates during the high-frequency cycles, focusing on the current control by PI controller to ensure fast response and precise adjustment. By integrating the slower BP neural network with the faster, more sensitive PI control, the DF-BPPI control

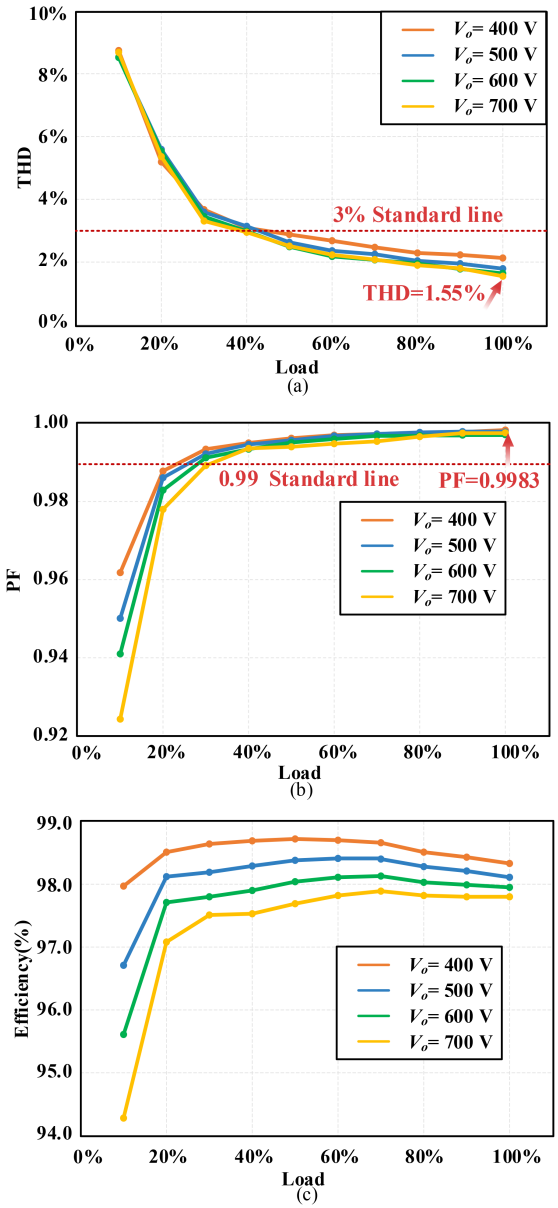

Fig. 20. Experimental results of the DF-BPPI control under different output voltages and loads. (a) THD-Load. (b) PF-Load. (c) Efficiency-Load.

Fig. 21. Screenshot of the power analyzer of prototype at 700 V output full load.

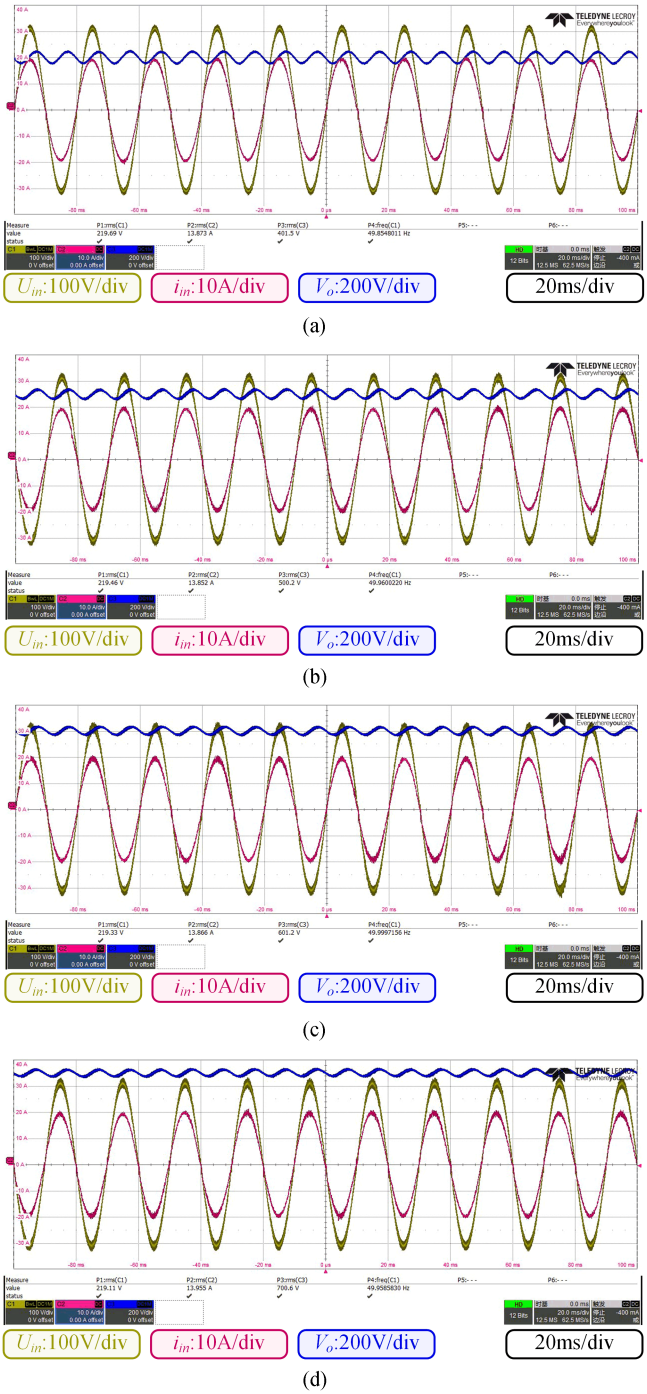

Fig. 22. Measured waveforms of the DF-BPPI at full load at different output voltages. (a) 400 V. (b) 500 V. (c) 600 V. (d) 700 V.

method achieves both fast response and parameter adaptation, solving the high current THD problem of traditional control over a wide range. The stability is primarily governed by the high-speed PI controller, since the BP neural network operating at a low-frequency cycle only adjusts the PI parameters and does not directly interfere with the dynamic response. Consequently, the stability characteristics of the DF-BPPI system resemble those of a fixed parameter PI controller, without introducing additional zeros or poles. The main distinction lies in the adjustment of the root locus due to parameter adaptation. As shown in Fig. 9, all closed-loop poles remain in the left half plane throughout the neural network training process, which ensures system stability under the proposed control method.

B. Forward and BP Calculation for the Designed Neural Network

The BP neural network first carries out forward propagation, and the relationship between the hidden layer and the input layer is as follows:

$$\begin{cases} \text{net}_j = \sum_{i=1}^{4} w_{ij} O_i & (i = 1, 2, 3) \\ O_j = f(\text{net}_j) & (j = 1, 2, 3, 4) \end{cases}. \tag{23}$$

The relationship between the hidden layer and the output layer is as follows:

$$\begin{cases} \text{net}_k = \sum_{j=1}^{4} w_{jk} O_j & (j = 1, 2, 3, 4) \\ O_k = f(\text{net}_k) & (k = 1, 2) \end{cases}. \tag{24}$$

The activation function is employed in both (13) and (14). Nonlinear factors are introduced to neurons, thereby enabling the neural network to arbitrarily approximate any nonlinear function, thus ensuring the network's applicability to nonlinear models. The activation function employed in the hidden and output layers is the Tanh function, with outputs ranging from -1 to 1. This is to ensure that the positive and negative correction of parameters can be achieved

$$f(x) = \tanh(x) = \frac{e^x - e^{-x}}{e^x + e^{-x}}. \tag{25}$$

The weight of the neural network is constantly updated in the negative gradient direction when the error is backpropagated. The implementation of this process is intended to minimize error and ensure low THD control

$$\Delta w_{jk}(m) = -\eta \frac{\partial \overline{E}(m)}{\partial w_{jk}} + \alpha \Delta w_{jk}(m-1) \tag{26}$$

$$\Delta w_{ij}(m) = -\eta \frac{\partial \overline{E}(m)}{\partial w_{ij}} + \alpha \Delta w_{ij}(m-1) \tag{27}$$

where η is the learning rate, representing the step size of the reverse search of the neural network, selecting an appropriate learning rate can make the network have both a higher convergence speed and a smaller oscillation; α is the inertia coefficient, selecting an appropriate inertia coefficient can make the network jump out of the local optimal solution to obtain better results. This article selects the classic values $\eta = 0.01$ and $\alpha = 0.6$ to construct the BP neural network. The derivative can be calculated using the chain rule as follows:

$$\frac{\partial \overline{E}(m)}{\partial w_{jk}} = \frac{\partial \overline{E}(m)}{\partial O_k(m)} \cdot \frac{\partial O_k(m)}{\partial net_k(m)} \cdot \frac{\partial net_k(m)}{\partial w_{jk}(m)} \tag{28}$$

$$\frac{\partial \overline{E}(m)}{\partial w_{ij}} = \frac{\partial \overline{E}(m)}{\partial O_k(m)} \cdot \frac{\partial O_k(m)}{\partial net_k(m)} \cdot \frac{\partial net_k(m)}{\partial O_j(m)} \cdot \frac{\partial O_j(m)}{\partial net_j(m)} \cdot \frac{\partial net_j(m)}{\partial w_{ij}(m)}. \tag{29}$$

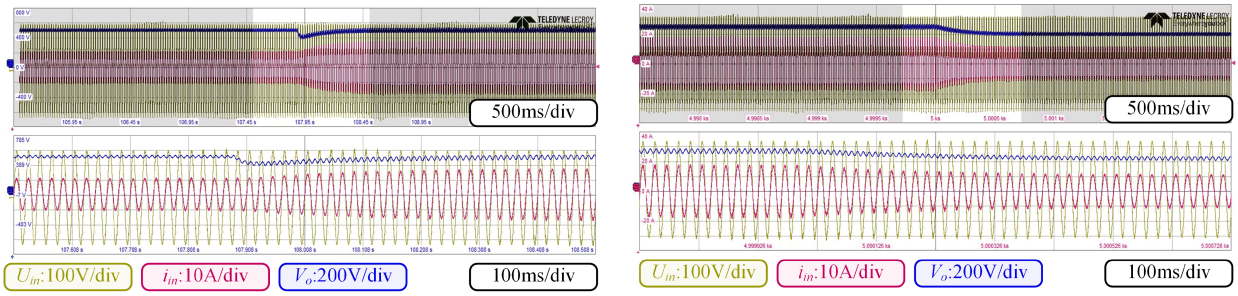

Fig. 23. Transient waveforms of the DF-BPPI. (a) Load step from 167 to 100 Ω. (b) Voltage step from 500 to 400 V.

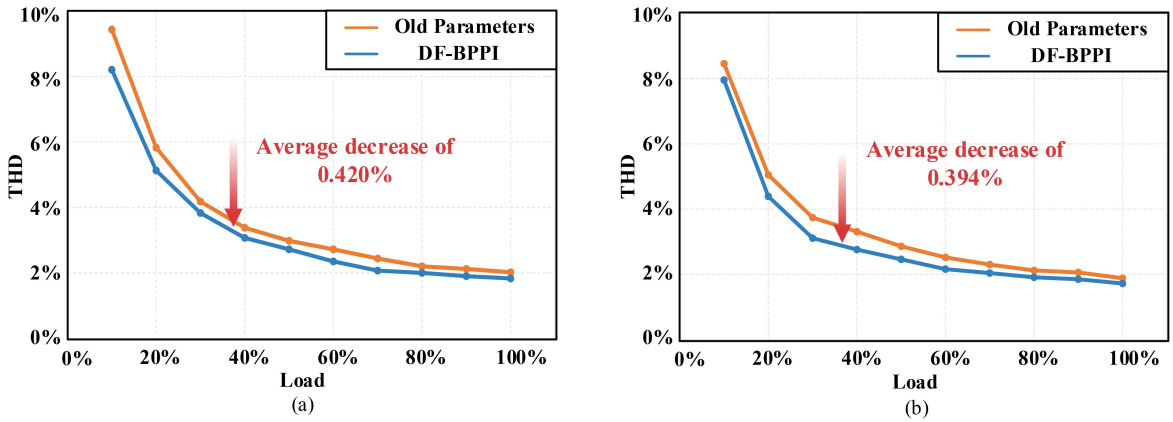

Fig. 24. THD comparison at different circuit parameters. (a) Inductance is 175 μH. (b) Inductance is 225 μH.

Considering that nonlinear derivatives are difficult to solve, approximate solutions are solved using symbolic functions:

$$\frac{\partial \overline{E}(m)}{\partial O_k(m)} \approx \operatorname{sgn}\left(\frac{\partial \overline{E}(m)}{\partial O_k(m)}\right) = \operatorname{sgn}\left(\frac{\overline{E}(m)-\overline{E}(m-1)}{O_k(m)-O_k(m-1)}\right). \tag{30}$$

Finally, the network weights updated by the backpropagation obtained by the solutions are as

$$\frac{\partial \overline{E}(m)}{\partial w_{jk}} = \operatorname{sgn}\left(\frac{\overline{E}(m)-\overline{E}(m-1)}{O_k(m)-O_k(m-1)}\right)\cdot f'(net_k(m))\cdot O_j(m) \tag{31}$$

$$\frac{\partial \overline{E}(m)}{\partial w_{ij}} = f'(net_j(m))\cdot O_i(m)\cdot \sum_{k=1}^{2}\left[\operatorname{sgn}\left(\frac{\overline{E}(m)-\overline{E}(m-1)}{O_k(m)-O_k(m-1)}\right)\cdot f'(net_k(m))\cdot w_{jk}(m)\right] \tag{32}$$

where the derivative of the activation function is

$$f'(x) = 1 - f^2(x). \tag{33}$$

C. Implementation of the Proposed Method

Fig. 15 shows the designed flow chart of DF-BPPI, where the blue flow represents the utility frequency control and the pink flow represents the high-frequency control.

First, the structure of the BP network is selected and the parameters of the neuron connection weights are initialized. Subsequently, the input network parameters are normalized, and BP and forward propagation calculations are performed. The PI parameters of the inner current loop are then updated based on these results, and new control error values are obtained through sampling. At each zero crossing of the power frequency cycle, the system evaluates whether the control meets the expected performance. If the optimal performance is not achieved, the network propagation calculation continues to adjust the PI parameters until the system stabilizes and the control error reaches the desired value, thereby concluding the process.

IV. Experimental Verifications

In order to evaluate the performance of the proposed control method, a three-phase OBC circuit was designed, as shown in Fig. 16.

The OBC prototype includes the totem pole PFC and LLC structure. As the main focus of this article is on the control of the totem pole PFC, the LLC circuit was disconnected and only the single-phase totem pole PFC was tested and analyzed. The main parameters of the circuit are shown in Table II. And the hardware connection block diagram is shown in Fig. 17. The hardware

TABLE II
PROTOTYPE PARAMETERS

Parameters	Values
Input AC voltage (V_{in})	220 V@50 Hz
Input AC current (i_L)	0–14 A
Output voltage (V_o)	350–700 V
Max Output power (P_{max})	3.0 kW
Switching frequency	75 kHz
Inductance (L)	200 μH
Output capacitance (C_o)	260 μF
Differential mode inductance	50 μH
Differential mode capacitance	4.4 μF
Controller	TMS320F28379S

TABLE III
COMPUTATIONAL RESOURCES TEST DATA

Process	Occupied time (μs)	Interruption time (μs)	Occupied computational resources
High-speed PI	4.12	33.33	12.36%
BP neural network	99.58	20000.00	0.50%
Voltage and current sampling	1.93	33.33	5.78%
Waveform generation	1.06	33.33	3.18%
Phase-locked loop	3.04	33.33	9.12%
Others (communication, protection, etc.)	2.16	33.33	6.48%
Total computational resources			37.42%
Remaining computational resources			62.58%

settings include two main circuits, the main power circuit, and the control circuit. The main power circuit includes 220 V rms, 50 Hz ac power supply, air switch, line filter, SiC-based power conversion module, and dc load. The control circuit has current and voltage sensors to obtain the actual measured value, and uses DSP to realize real-time control.

TMS320F28379S DSP is selected as the controller, and the main frequency is set to 150 MHz. Table III shows the computational resources of the experimental test, and the total computational resources are about 37.42%. The proposed method does not require additional hardware costs. BP neural network works in a low-frequency cycle and occupies low computational resources, so the proposed method is suitable for the deployment of embedded systems.

In the comparison experiments, the parameters set at 700 V output voltage are used as traditional fixed PI control, which is compared with the DRL-PI control proposed in Section II and the DF-BPPI control proposed in Section III. The input current THD data was collected by the power analyzer PA5000H to evaluate the control effect. The measurement bandwidth of the power analyzer is 5 M and the sampling rate is 2 MS/s. Fig. 18(a) shows the THD comparison of different control methods under different loads when the output voltage is 400 V. Fig. 18(b) shows the THD comparison of different control methods under different output voltages when the resistance is 160 Ω.

It is evident that the control performance of the traditional fixed PI deteriorates when the voltage deviates from the set condition. Furthermore, the larger the output voltage deviation, the worse the control effect. Although DRL-PI control can adjust control parameters based on inductance and output voltage, it cannot achieve optimal control performance due to parasitic parameters, control delay, temperature changes, and other factor. This means that even at the nominal point, the optimal parameter control of the theory is still difficult to maintain the optimal performance. In contrast, DF-BPPI showed better robustness in the experiment. The DF-BPPI method solves this problem by compensating the influence of complex factors, current THD decreases in the whole working range. It can achieve adaptive control under a wide operating condition, effectively reducing current THD. Compared with the fixed PI control, for the 400 V constant voltage output, THD decreased by 10.4% under the 10% load and by 5.2% under the 100% load, for the 160 Ω constant load, THD decreased by 5.1% under the 350 V output and by 0.7% under the 700 V output.

In addition, due to the great harm of odd harmonics to the power grid, this article tested the odd harmonics analysis comparison data of traditional control and DF-BPPI control under 700 V full load output, as shown in Fig. 19. It can be seen that the proposed control can effectively reduce the harmonic components of each order.

To further assess the wide-range control capability of the method proposed in this article, DF-BPPI was tested under different output voltages and loads. The resulting THD-Load curves, PF-Load, and Efficiency-Load curves are shown in Fig. 20. Experimental results show that the DF-BPPI control method achieves a THD of less than 3% and a PF higher than 0.995 under all output voltages above half load. Fig. 21 shows a screenshot of the power analyzer at 700 V full load, achieving the best results with THD = 1.55% and PF = 0.9983. Fig. 22 shows the waveforms of the DF-BPPI control at full load at different output voltages.

Then, Fig. 23(a) shows the transient waveform when the load steps from 167 Ω (1.5 kW) to 100 Ω (2.5 kW) under 500 V constant voltage output. Fig. 23(b) shows the transient waveform of the output voltage from 500 to 400 V under a 100 Ω constant resistance output. After the transient behavior, the high-speed PI control ensures the stable operation of the system. The low-speed BP neural network control is then reactivated after detecting the increase of THD in the system, and the process in Fig. 15 is repeated for parameters correction to achieve the optimal current THD control in the steady state.

Finally, the inductance of the totem pole PFC is changed to verify the adaptability to the circuit parameters. The parameters set by DF-BPPI when the inductance was 200 μH were selected as the fixed parameters control group, and real-time DF-BPPI control was used for comparative analysis. THD-Load curves obtained under different inductors are shown in Fig. 24. When the inductance is 175 μH, the average THD decreased by 0.420%, and when the inductance is 225 μH, the average THD decreased by 0.394%. This proves that the DF-BPPI control

TABLE IV
COMPARISON OF DIFFERENT CONTROL METHOD

	This work	[12]	[13]	[14]	[16]
Method	DF-BPPI	Traditional	LQR	PI-Fuzzy	HOSMC
Steady-state performance	Excellent	Poor	Excellent	Moderate	Excellent
Robustness	Excellent	Poor	Moderate	Moderate	Excellent
Complexity	Moderate	Simple	Moderate	Moderate	Complex
Feasibility	High	High	High	High	Low

method can adjust control parameters according to changes in circuit parameters, achieving lower current THD control.

Furthermore, Table IV gives a comparison of different control methods in terms of steady-state performance, robustness, complexity, and feasibility. Overall, the method proposed in this article enables efficient wide-range adaptive control of totem pole PFC on digital controllers with limited computational capabilities.

V. CONCLUSION

This article proposes a dual frequency parameter adjustment method to solve the problem of large current THD of totem pole PFC topology in a wide operating range. By combining a slow-speed BP neural network with high-speed PI current control, this method can utilize the limited computational resources of the controller to adjust control parameters and achieve optimal control. In addition, the adjustment of parameters is based on the PI control designed by the dynamic root locus, which improves the stability and robustness of the system.

Experimental results have verified that compared to traditional methods, the proposed DF-BPPI method reduced THD by 5.82% on average at a constant output voltage and achieved THD lower than 3% under all output voltages above half load.

REFERENCES

[1] V. I. Silaev, O. A. Gavrina, and A. V. Kuzina, "The problem of renewable energy sources and market mechanisms in various energy systems in the era of global crises," in *Proc. Int. Ural Conf. Elect. Power Eng.*, 2023, pp. 83–88.

[2] H. Wouters and W. Martinez, "Bidirectional onboard chargers for electric vehicles: State-of-the-art and future trends," *IEEE Trans. Power Electron.*, vol. 39, no. 1, pp. 693–716, Jan. 2024.

[3] T. Li et al., "Design and optimization of a high efficiency energy router," in *Proc. 4th Energy Convers. Econ. Annu. Forum*, 2025, pp. 1154–1158.

[4] T. Liu, C. Chen, K. Xu, Y. Zhang, and Y. Kang, "GaN-based megahertz single-phase inverter with a hybrid TCM control method for high efficiency and high-power density," *IEEE Trans. Power Electron.*, vol. 36, no. 6, pp. 6797–6813, Jun. 2021.

[5] J. Guan, Z. Wang, Z. Tang, J. Lv, C. Chen, and Y. Kang, "Design of a high power density bidirectional AC/DC converter based on GaN," in *Proc. IEEE Workshop Wide Bandgap Power Devices Appl. Asia*, 2021, pp. 393–397.

[6] P. Mohseni, O. Husev, D. Vinnikov, R. Strzelecki, E. Romero-Cadaval, and I. Tokarski, "Battery technologies in electric vehicles: Improvements in electric battery packs," *IEEE Ind. Electron. Mag.*, vol. 17, no. 4, pp. 55–65, Dec. 2023.

[7] Y. Wei and P. Sun, "Review of techniques for resonant converters with wide voltage gain range applications," *IEEE Trans. Transp. Electrific.*, vol. 10, no. 3, pp. 5544–5569, Sep. 2024.

[8] H. Wang, S. Dusmez, and A. Khaligh, "Maximum efficiency point tracking technique for LLC-based PEV chargers through variable DC link control," *IEEE Trans. Ind. Electron.*, vol. 61, no. 11, pp. 6041–6049, Nov. 2014.

[9] A. Kazemtarghi, N. Ishraq, P. Rathod, A. Mallik, and N. Johnson, "DC link voltage optimization for efficiency enhancement of electric vehicle onboard chargers," in *Proc. IEEE 2nd Ind. Electron. Soc. Annu. -Line Conf.*, 2023, pp. 1–6.

[10] M. A. Qureshi, S. Musumeci, F. Torelli, A. Reatti, A. Mazza, and G. Chicco, "Application of advanced model reference adaptive control for bidirectional AC-DC converters," in *Proc. 58th Int. Universities Power Eng. Conf.*, 2023, pp. 1–5.

[11] *Electromagnetic Compatibility, Part 3–2: Limits—Limits for Harmonic Current Emissions (Equipment Input Current 16 A Per Phase)*, IEC Standard 61000-3-2, 2018.

[12] C. Song and H. Li, "Evaluation of efficiency and power factor in 3-kW GaN-based CCM/CRM totem-pole PFC converters for data center application," in *Proc. 11th Int. Conf. Power Electron. ECCE Asia*, 2023, pp. 2663–2668.

[13] W. Jiao, Y. Gao, W. Yan, S. Wu, F. Gao, and X. Yang, "Simulation analysis of totem pole PFC using steady error free quadratic optimal PID control," in *Proc. 11th Int. Conf. Power Energy Syst.*, 2021, pp. 290–294.

[14] K. Sayed and H. A. Gabbar, "Electric vehicle to power grid integration using three-phase three-level AC/DC converter and pi-fuzzy controller," *Energies*, vol. 9, no. 7, pp. 532, 2016.

[15] R. Sabzehgar, Y. M. Roshan, and P. Fajri, "Modelling and sliding-mode control of a single-phase single-stage converter with application to plug in electric vehicles," *IET Power Electron.*, vol. 12, no. 3, pp. 620–626, 2019.

[16] Y. Shtessel, M. Taleb, and F. Plestan, "A novel adaptive-gain supertwisting sliding mode controller," *Methodol. Appl., Automatica*, vol. 48, no. 5, pp. 759–769, 2012.

[17] S. Zhao, F. Blaabjerg, and H. Wang, "An overview of artificial intelligence applications for power electronics," *IEEE Trans. Power Electron.*, vol. 36, no. 4, pp. 4633–4658, Apr. 2021.

[18] A. S. Soliman, S. M. S. H. Rafin, and O. A. Mohammad, "Enhanced DC voltage and power regulation using intelligent data-driven control for AC/DC converters in DC microgrid applications," *IEEE Trans. Ind. Appl.*, vol. 60, no. 6, pp. 8383–8392, Nov./Dec. 2024.

[19] A. S. Soliman, M. M. Amin, F. F. M. El-Sousy, and O. A. Mohammad, "Experimental validation for artificial data-driven tracking control for enhanced three-phase grid-connected boost rectifier in DC microgrids," *IEEE Trans. Ind. Appl.*, vol. 59, no. 2, pp. 2563–2580, Mar./Apr. 2023.

[20] X. Zhou, W. Wang, and Y. Shi, "Neural network/PID adaptive compound control based on RBFNN identification modeling for an aerial inertially stabilized platform," *IEEE Trans. Ind. Electron.*, vol. 71, no. 12, pp. 16514–16522, Dec. 2024.

[21] H. Huang and Z. Chen, "Current control of EAST fast control power supply based on single neuron adaptive predictive PI," in *Proc. IEEE 6th Int. Elect. Energy Conf.*, 2023, pp. 89–94.

[22] L. Li and M. Luo, "Research on an improved single neuron PI control strategy," in *Proc. Int. Conf. Comput. Netw., Electron. Autom.*, 2020, pp. 409–413.

[23] A. Z. Badr, "Neural network based adaptive PID controller," *IFAC Proc. Volumes*, vol. 30, no. 6, pp. 251–257, 1997.

[24] Y. Zhang et al., "A PI self-tuning method for three-phase PWM rectifiers based on stability-and-dynamics- constrained fuzzy backpropagation neural network," *IEEE Trans. Power Electron.*, vol. 40, no. 1, pp. 2419–2428, Jan. 2025.

[25] B. H. Ren, G. Zhou, L. Shen, C. Wei, and Q. Li, "Variable pitch active disturbance rejection control of wind turbines based on BP neural network PID," *IEEE Access*, vol. 8, pp. 71782–71797, 2020.

[26] T. Li, C. Huo, F. Zeng, J. Ding, and Y. Huang, "Design of PID control algorithm for mechanical arm based on BP neural network model," in *Proc. 2nd Int. Conf. Artif. Intell. Auton. Robot. Syst.*, 2023, pp. 406–409.

[27] M. Sun, "Research on PID control of BP neural networks based on PSO optimization," in *Proc. IEEE 2nd Int. Conf. Control, Electron. Comput. Technol.*, 2024, pp. 733–738.

[28] L. Huber, M. Kumar, and M. M. Jovanović, "Performance comparison of PI and P compensation in DSP-based average-current-controlled three-phase six-switch boost PFC rectifier," *IEEE Trans. Power Electron.*, vol. 30, no. 12, pp. 7123–7137, Dec. 2015.
[29] G. C. Goodwin, S. F. Graebe, and M. E. Salgado, *Control System Design*, 1st ed. Englewood Cliffs, NJ, USA: Prentice Hall, 2000.
[30] Y. Zhao, X. Wang, and M. Wang, "On the backward Euler method for a generalized Ait-Sahalia-type rate model with Poisson jumps," *Numer. Algorithms*, vol. 87, pp. 1321–1341, 2021.

Hao Chu received the B.S. degree in electrical engineering and automation, in 2024, from the School of Electrical and Electronic Engineering, Huazhong University of Science and Technology, Wuhan, China, where he is currently working toward the Ph.D. degree in electrical engineering.

His research interests include power electronic automation control, application of artificial intelligence in power electronics, and modulation of DAB topology.

Jiajia Guan (Member, IEEE) received the B.S. degree in electrical and electronic engineering from Dalian Maritime University, Dalian, China, in 2020, and the Ph.D. degree in electrical engineering and electronic engineering from Huazhong University of Science and Technology, Wuhan, China, in 2025.

He is currently conducting postdoctoral research with the School of Electrical and Electronic Engineering, Huazhong University of Science and Technology. His current research interests include high efficiency and high power density converter, magnetic integration, and applications of wide bandgap powers.

Xuchen Sun received the B.S. degree in theoretical physics, in 2023, from the School of Physics, Huazhong University of Science and Technology, Wuhan, China, where he is currently working toward the Ph.D. degree in electrical engineering from the School of Electrical and Electronic Engineering.

His current research interests include high power dc/ac converter and three-port dc–dc converter.

Xiangan Xiao received the B.S. degree in electrical engineering and automation in 2025 from the School of Electrical and Electronic Engineering, Huazhong University of Science and Technology, Wuhan, China, where he is currently working toward the M.S. degree in electrical engineering.

His research interests include high-efficiency and high power density isolated dc–dc conversion and application of wide bandgap power semiconductor devices.

Letian Tong received the B.S. degree in electrical engineering and automation from Hunan University, Changsha, China, in 2020, and the M.S. degree in electrical engineering and automation from the School of Electrical and Electronic Engineering, Huazhong University of Science and Technology, Wuhan, China, in 2025.

His research interests include active gate drivers, power semiconductor devices, and applications of wide bandgap power semiconductor devices.

Xinyu He (Student Member, IEEE) received the B.S. degree in electrical engineering and automation from the China University of Petroleum, Beijing, China, in 2024. She is currently working toward the master's degree in electrical engineering with the School of Electrical and Electronic Engineering, Huazhong University of Science and Technology Wuhan, China.

Her research interests include high-frequency power conversion techniques and applications of wide bandgap power semiconductor devices.

Cai Chen (Member, IEEE) received the B.S. and Ph.D. degrees in electrical and electronic engineering from Huazhong University of Science and Technology, Wuhan, China, in 2008 and 2014, respectively.

He is a Professor with Huazhong University of Science and Technology, Wuhan, China. From 2013 to 2013, he was an Intern in GE Global Research Center, Shanghai, China. From 2014 to 2016, he joined the Advanced Semiconductor, Packaging and Integration Lab, Huazhong University of Science and Technology, Wuhan, China, as a Postdoctoral Researcher. From 2016 to Oct. 2017, he was a Visiting Scholar with the Center for High Performance Power Electronics, The Ohio State University, Columbus, OH, USA. From 2017 to Oct. 2018, he was a Visiting Scholar with the College of Engineering, University of Arkansas, Fayetteville, AR, USA. In 2019, he joined the Huazhong University of Science and Technology, Wuhan, China, as an Associate Research Fellow. His research interests include WBG devices packaging, integration, packaging EMI issues, packaging reliability, and high-density applications.

Yong Kang (Fellow, IEEE) was born in Hubei Province, China, on October 16, 1965. He received the B.E. M.E, and Ph.D. degrees from Huazhong University of Science and Technology, Wuhan China, in 1988, 1991, and 1994, respectively.

In 1994, he joined Huazhong University of Science and Technology as a Lecturer and was promoted to Associate Professor, in 1996, and to Full Professor, in 1998. He has authored more than 60 technical papers. His research interests include power electronic converter, ac drivers, electromagnetic compatibility, their digital control techniques, WBG device packaging, and applications.